AIAA Aviation
13-17 June 2016, Washington, D.C.
8th AIAA Atmospheric and Space Environments Conference

A High-Order Multiscale Global Atmospheric Model

Ram D. Nair*
National Center for Atmospheric Research, Boulder, CO 80305, USA.
Lei Bao†
Department of Applied Mathematics, University of Colorado at Boulder, CO 80305, USA.
Michael D. Toy‡
National Center for Atmospheric Research, Boulder, CO 80305, USA.
Robert Kloefkorn §
International Research Institute of Stavanger, Stavanger, Norway

The High-Order Method Modeling Environment (HOMME), developed at NCAR, is a petascale hydrostatic framework, which employs the cubed-sphere grid system and high-order continuous or discontinuous Galerkin (DG) methods. Recently, the HOMME framework is being extended to a non-hydrostatic dynamical core known as the High-Order Multiscale Atmospheric Model (HOMAM). The spatial discretization is based on DG or high-order finite-volume methods. Orography is handled by the terrain-following height-based coordinate system. To alleviate the stringent CFL stability requirement resulting from the vertical aspects of the dynamics, an operator-splitting time integration scheme based on the horizontally explicit and vertically implicit (HEVI) philosophy is adopted for HOMAM. Preliminary results with the benchmark test cases proposed in the Dynamical Core Model Intercomparison project (DCMIP) test suite are encouraging.

I. Introduction

Atmospheric numerical modeling has been going through revolutionary changes over the past decade. One major reason for this trend is the recent paradigm change in scientific computing, triggered by the advent of petascale computing resources with core counts in the tens of thousands to hundreds of thousands range. Modern atmospheric modelers must adapt grid systems and numerical algorithms to facilitate an unprecedented level of scalability on these modern, highly parallel computer architectures. The numerical algorithms which can address these challenges should have local properties such as high on-processor floating-point operation count and minimum parallel communication footprint. The dynamical core is the central component of every climate and weather research model. It encompasses the numerical methods used to solve the equations of motion on the resolved scales. Since the target resolutions for global modeling is nearing the non-hydrostatic scale (of the order of a few km in the horizontal), the equation set generally used in climate models are based on the compressible Euler equations or Navier-Stokes equations.

To meet the challenges of building a new generation of atmospheric general circulation models, the National Center for Atmospheric Research (NCAR) has developed a computationally efficient and scalable atmospheric modeling framework known as the High-Order Method Modeling Environment (HOMME). For the spatial discretization, HOMME primarily employs the spectral-element[1] and discontinuous Galerkin (DG) methods[2] on a cubed-sphere tiled with quadrilateral elements. The DG method has several computationally attractive properties, which include local conservation, geometric flexibility, high-order accuracy and high-parallel efficiency.

*Scientist, CISL/IMAGe, rnair@ucar.edu.
†Graduate Student, CU Boulder, lei.bao@colorado.edu
‡Scientist, CISL/IMAGe, toy@ucar.edu.
§Scientist, IRIS, robert.kloefkorn@iris.no.

Recently, the HOMME framework is being extended to a non-hydrostatic (NH) dynamical core – the "High-Order Multiscale Atmospheric Model" (HOMAM). Since the DG method possesses computationally desirable properties, such as local and global conservation, geometric flexibility, high on-processor operations and minimal communication footprints, it is used as the basic spatial discretization scheme for the HOMAM. Traditionally, 3D global NH models are developed in a dimension-split manner, which combines the horizontal 2D (spherical surface) and vertical 1D domains, using various standard discretization techniques.[3,4,5] A major reason for this is the ease of implementing various semi-implicit time integration schemes, which alleviates the stringent CFL stability requirement resulting from the vertical aspects of the dynamics. Although the DG method can handle 3D elements,[6,7] we prefer to use the conventional dimension-split approach for HOMAM.

A major challenge for global NH modeling is to develop a practical time-stepping method. By nature the physical domain of the atmosphere is a shallow spherical shell with a horizontal length scale of $O(10,000)$ km and a vertical length scale of $O(10)$ km. Computationally this makes the problem very challenging. The high aspect ratio between horizontal and vertical grid spacing combined with fast-moving acoustic waves impose a stringent stability constraint for explicit time stepping. A recent study[8] introduces a time-splitting approach for a DG 2D-NH model based on the compressible Navier-Stokes system. This time integration is based on so-called horizontally-explicit and vertically-implicit (HEVI) methods and relies on the Strang-type operator-split philosophy. An important feature of this scheme is that the model time stepping is independent of the vertical resolution, and is limited only by the horizontal Courant number. As a first step, the HEVI time-step has recently been extended to the HOMAM 3D advection scheme[9] and found to be accurate and efficient. Our goal is to extend the HEVI scheme to the HOMAM framework for practical NH dynamics.

The Dynamical Core Model Intercomparison Project (DCMIP)[10] provides a set of benchmark test cases for validating global NH atmospheric models. For the current study, we are particularly interested a challenging advection test-case[11] and a couple idealized 3D NH tests from the DCMIP test-suite for validating the HOMAM dynamical core. In this paper we further validate HOMAM dynamics and the HEVI time integration scheme with NH tests as well as the accuracy of spatial discretization with terrain-following vertical coordinate using benchmark tests proposed in DCMIP test suite.

II. High-Order Multiscale Atmospheric Model (HOMAM)

Total mass and energy conservation is extremely important for climate scale integration, therefore, in our formulation we adopt the following flux-form of the compressible Navier-Stokes system. Typically, the 3D wind vector $\mathbf{V}$, density ρ, potential temperature θ and moisture variables q_k are used as the prognostic variables.[12,13] Upon splitting the density and pressure as $\rho = \overline{\rho} + \rho'$ and $p = \overline{p} + p'$, where the mean values $\overline{\rho}$ and $\overline{p}$ are in hydrostatic balance $\partial\overline{p}/\partial z = -\overline{\rho}g$, we have the flux-from governing equations in the following general form:

$$\frac{\partial \rho}{\partial t} + \nabla \cdot (\rho \mathbf{V}) = 0 \tag{1}$$

$$\frac{\partial \rho \mathbf{V}}{\partial t} + \nabla \cdot (\rho \mathbf{V} \otimes \mathbf{V}) = -\nabla p' - \rho' g \hat{\mathbf{k}} - 2\rho \boldsymbol{\Omega} \times \mathbf{V} + \mathbf{F}_M \tag{2}$$

$$\frac{\partial \rho \theta}{\partial t} + \nabla \cdot (\rho \theta \, \mathbf{V}) = 0 \tag{3}$$

$$\frac{\partial \rho q}{\partial t} + \nabla \cdot (\rho \, q \mathbf{V}) = 0 \tag{4}$$

where $(2\rho\boldsymbol{\Omega} \times \mathbf{V})$ is the Coriolis force term, $\mathbf{F}_M$ is the forcing term including the diffusive fluxes, $\boldsymbol{\Omega}$ is Earth's angular velocity, $\hat{\mathbf{k}}$ is the radial unit vector, g is gravity, and q is a passive tracer field. The potential temperature θ is related to the real temperature T by $\theta = T(p_0/p)^{R_d/c_p}$. The above system is closed by the equation of state, $p = C_0(\rho\theta)^\gamma$ where $C_0 = R_d^\gamma p_0^{-R_d/c_v}$. The reference surface pressure $p_0 = 10^5$ Pa, and the other thermodynamic constants are given by $\gamma = c_p/c_v$, R_d =287 J kg^{-1} K^{-1}, c_p = 1004 J kg^{-1} K^{-1} and c_v = 717 J kg^{-1} K^{-1}.

A. Governing Equations on the Cubed Sphere

The physical domain is a sphere $\mathcal{S}$, representing the planet Earth, based on the cubed-sphere topology.[14] Here we consider the cubed-sphere geometry employing the equiangular central projection as described in Nair et

al.[15] The cubed-sphere geometry consists of partitioning $\mathcal{S}$ into six identical regions which are obtained by the central projection of the faces of the inscribed cube onto the surface of $\mathcal{S}$. Each of the local coordinate systems is free of singularities, employs identical metric terms, and creates a non-orthogonal curvilinear coordinate system on $\mathcal{S}$. However, the edges of the faces are discontinuous. The local coordinates (or central angles of the projection) for each face are $x^1 = x^1(\lambda, \phi)$, $x^2 = x^2(\lambda, \phi)$ such that $x^1, x^2 \in [-\pi/4, \pi/4]$, where λ and ϕ are the longitude and latitude, respectively, of a sphere with radius r. The metric (second-order) tensor, G_{ij} associated with the transformation is

$$G_{ij} = \frac{r^2}{\mu^4 \cos^2 x^1 \cos^2 x^2} \begin{bmatrix} 1 + \tan^2 x^1 & -\tan x^1 \tan x^2 \\ -\tan x^1 \tan x^2 & 1 + \tan^2 x^2 \end{bmatrix}, \tag{5}$$

where $i, j \in \{1, 2\}$ and $\mu^2 = 1 + \tan^2 x^1 + \tan^2 x^2$. The Jacobian of the transformation (the metric term) is $\sqrt{G}_h = [\det(G_{ij})]^{1/2}$.

The momentum equations are treated in tensor form with covariant (u_i) and contravariant (u^i) wind vectors, which are related through $u_i = G_{ij}u^j$, $u^i = G^{ij}u_j$ and $G^{ij} = G_{ij}^{-1}$. The orthogonal components of the spherical wind vector $\mathbf{v}(\lambda, \phi) = (u, v)$ can be expressed in terms of contravariant vectors (u^1, u^2) as follows,

$$\begin{bmatrix} u \\ v \end{bmatrix} = \mathbf{A} \begin{bmatrix} u^1 \\ u^2 \end{bmatrix}, \quad \mathbf{A} = \begin{bmatrix} r\cos\theta\, \partial\lambda/\partial x^1 & r\cos\theta\, \partial\lambda/\partial x^2 \\ r\, \partial\theta/\partial x^1 & r\, \partial\theta/\partial x^2 \end{bmatrix}; \quad \mathbf{A}^T\mathbf{A} = G_{ij}. \tag{6}$$

The details of the local transformation laws and $\mathbf{A}$ for each face of the cubed-sphere can be found in Nair et al.[15] The cubed-sphere geometry provides quasi-uniform rectangular tiling on the sphere with six subdomains with analytic metric terms, which is suitable for high-order element-based Galerkin methods such as DG.[2]

In order to mathematically represent the atmosphere (a 3D spherical shell), we need to consider an independent variable x^3 in the radial direction ($\vec{r}$) with respect to the cubed-sphere. However, with the shallow atmosphere approximation, for which $x^3 = r + z$ and $z \ll r$, where z is the geometrical height above the surface, the resulting governing equations can be simplified. The shallow atmosphere approximation allows treating the vertical levels of the discretized model as vertically stacked layers, while keeping the radius (r) of the planet as a constant. The 3D governing equations (1)-(4), without diffusive fluxes, in non-orthogonal curvilinear cubed-sphere coordinates (x^j) can be written in the following tensor form (summation implied):[16]

$$\frac{\partial \rho}{\partial t} + \frac{1}{\sqrt{G}}\left[\frac{\partial}{\partial x^j}(\sqrt{G}\,\rho u^j)\right] = 0 \tag{7}$$

$$\frac{\partial \rho u^i}{\partial t} + \frac{1}{\sqrt{G}}\left[\frac{\partial}{\partial x^j}[\sqrt{G}(\rho u^i u^j + p\, G^{ij})]\right] = -\Gamma^i_{jk}(\rho u^j u^k + p\, G^{jk}) + f\sqrt{G}(u^1 G^{2i} - u^2 G^{1i}) - \rho g\, G^{3i} \tag{8}$$

$$\frac{\partial \rho\theta}{\partial t} + \frac{1}{\sqrt{G}}\left[\frac{\partial}{\partial x^j}(\sqrt{G}\,\rho\theta\, u^j)\right] = 0 \tag{9}$$

$$\frac{\partial \rho q}{\partial t} + \frac{1}{\sqrt{G}}\left[\frac{\partial}{\partial x^j}(\sqrt{G}\,\rho q\, u^j)\right] = 0, \tag{10}$$

where u^i is the contravariant wind field and f is the Coriolis parameter. Γ^i_{jk} is the associated Christoffel symbols of the second kind,[17] and the details are provided in the Appendix. Note that with the shallow atmosphere approximation $x^3 \Rightarrow z$, and the Jacobian $\sqrt{G} = \sqrt{G}_h$.

B. Inclusion of topography

The shallow atmosphere approximation allows treating the vertical levels of the discretized model as vertically stacked layers while considering the radius (r) of the planet as a constant. As a primary step, we follow this assumption for HOMAM, which simplifies the governing equations in curvilinear system to some extent. This implies that the vertical levels of the cubed sphere will have the same horizontal metric terms. Since the horizontal aspects remains the same, we use the same notational convention for the 3D system.

HOMAM employs the shallow atmosphere approximation, i.e., $x^3 = r + z$ and $z \ll r$, where r is the Earth's radius and z is the vertical height. The vertical grid system relies on the height-based terrain-following coordinate $\zeta = z(\zeta)$[18] such that $z \in [h_s, z_{top}]$, where h_s is bottom topography and z_{top} is the

prescribed top boundary of the model; the vertical velocity is then given by $w = dz/dt$. A dimension-split (2D + 1D) approach allows for the treatment of the 3D atmosphere as vertically-stacked cubed-sphere layers ($\mathcal{S}$) in the z direction,[9] as schematically shown in Fig.1.

The Euler system defined above can be written in the following compact form:

$$\frac{\partial \mathbf{U}}{\partial t} + \frac{\partial \mathbf{F}_1}{\partial x^1} + \frac{\partial \mathbf{F}_2}{\partial x^2} + \frac{\partial \mathbf{F}_3}{\partial \zeta} = \mathbf{S}(\mathbf{U}), \tag{11}$$

where $\mathbf{U}$ is the state vector and $\mathbf{F}_1, \mathbf{F}_2, \mathbf{F}_3$ are the flux functions along the coordinates and $\mathbf{S}(\mathbf{U})$ denote the source vector. These are defined as follows:

$$\mathbf{U} = \begin{bmatrix} \sqrt{G}\rho' \\ \sqrt{G}\rho u^1 \\ \sqrt{G}\rho u^2 \\ \sqrt{G}\rho w \\ \sqrt{G}(\rho\theta)' \end{bmatrix} \tag{12}$$

$$\mathbf{F}_1 = \begin{bmatrix} \sqrt{G}\,\rho u^1 \\ \sqrt{G}\,(\rho u^1 u^1 + p' G_h^{11}) \\ \sqrt{G}\,(\rho u^2 u^1 + p' G_h^{21}) \\ \sqrt{G}\,\rho w u^1 \\ \sqrt{G}\,\rho\theta u^1 \end{bmatrix} \tag{13}$$

$$\mathbf{F}_2 = \begin{bmatrix} \sqrt{G}\,\rho u^2 \\ \sqrt{G}\,(\rho u^1 u^2 + p' G_h^{12}) \\ \sqrt{G}\,(\rho u^2 u^2 + p' G_h^{22}) \\ \sqrt{G}\,\rho w u^2 \\ \sqrt{G}\,\rho\theta u^2 \end{bmatrix} \tag{14}$$

$$\mathbf{F}_3 = \begin{bmatrix} \sqrt{G}\,\rho\tilde{w} \\ \sqrt{G}\,\rho u^1\tilde{w} + \sqrt{G}_h\,(\sqrt{G}_v G_v^{13}\,G_h^{11}p' + \sqrt{G}_v G_v^{23}\,G_h^{12}p') \\ \sqrt{G}\,\rho u^2\tilde{w} + \sqrt{G}_h\,(\sqrt{G}_v G_v^{13}\,G_h^{21}p' + \sqrt{G}_v G_v^{23}\,G_h^{22}p') \\ \sqrt{G}\,\rho w\tilde{w} + \sqrt{G}_h p' \\ \sqrt{G}\,\rho\theta\tilde{w} \end{bmatrix} \tag{15}$$

$$\mathbf{S}(\mathbf{U}) = \sqrt{G}\begin{bmatrix} 0 \\ \sqrt{G}_h\,\rho f(u^1 G^{21} - u^2 G^{11}) - M_\Gamma^1 \\ \sqrt{G}_h\,\rho f(u^1 G^{22} - u^2 G^{12}) - M_\Gamma^2 \\ -\rho' g \\ 0 \end{bmatrix} \tag{16}$$

The computational domain for the Euler system (7-10) comprises the 3D coordinate system (x^1, x^2, z), with $w = u^3 = dz/dt$. The vertical coordinate transformation $z \to \zeta$ invariably introduces vertical metric terms. In order to simplify notations, let us consider the following definitions separately for the horizontal (cubed-sphere) and the vertical ζ-coordinate systems. The Jacobian of the horizontal transformation is denoted as $\sqrt{G_h} \equiv \sqrt{\det(G_{ij})}$; let the Jacobian associated with $z \to \zeta$ transformation be $\sqrt{G_v}$. Let $\sqrt{G} = \sqrt{G_h}\,\sqrt{G_v}$ be the *composite* metric term required for deriving the Euler system in (x^1, x^2, ζ) coordinates. Similarly the notations G_h^{ij} and G_v^{ij} are the contravariant terms associated with the horizontal and vertical transformations, respectively.

The computational domain defined by (x^1, x^2, ζ) coordinates may be viewed as a combination of two transformations: $(x, y, z) \to (x^1, x^2, z) \to (x^1, x^2, \zeta)$. To do that, we first convert the 3D Euler Cartesian system from $(x, y, z) \to (x^1, x^2, z)$, in the cubed-sphere horizontal coordinates, and then we perform the transform[18] from $(x^1, x^2, z) \to (x^1, x^2, \zeta)$.

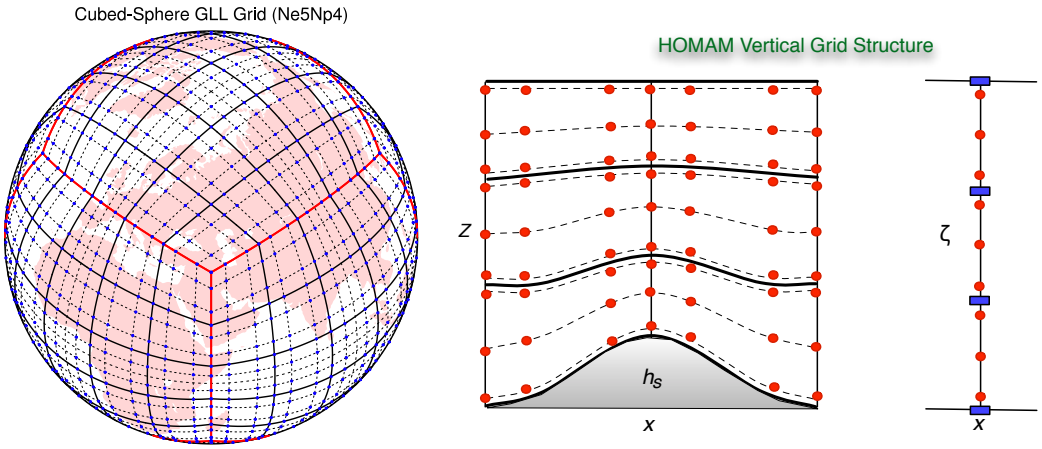

Figure 1. Schematic diagram showing the horizontal and vertical grid structure of the model. The horizontal grid system relies on the cubed-sphere (left panel) tiled with GLL quadrature elements stacked in the vertical z-direction. The right panel shows the vertical placement of horizontal levels with 1D elements using the terrain-following vertical coordinates $\zeta = \zeta(z)$.

Let $h_s = h_s(x^1, x^2)$ be the prescribed mountain profile and z_{top} the top of the model domain. The vertical z height coordinate can then be transformed to the monotonic ζ coordinate using the following mapping:

$$\zeta = z_{top}\frac{z - h_s}{z_{top} - h_s}, \quad z(\zeta) = h_s(x^1, x^2) + \zeta\,\frac{z_{top} - h_s}{z_{top}}; \quad h_s \le z \le z_{top}. \tag{17}$$

The Jacobian associated with the transform $(x^1, x^2, z) \to (x^1, x^2, \zeta)$ is

$$\sqrt{G}_v = \left[\frac{\partial z}{\partial \zeta}\right]_{(x^1,x^2)} = 1 - \frac{h_s(x^1, x^2)}{z_{top}} \tag{18}$$

The vertical velocity in the ζ coordinate is $\tilde{w} = d\zeta/dt$ and is related to w[19] via the chain rule, i.e.,

$$\sqrt{G}_v\tilde{w} = w + \sqrt{G}_v G_v^{13}\,u^1 + \sqrt{G}_v G_v^{23}\,u^2, \tag{19}$$

where the metric coefficients are defined as follows:

$$\sqrt{G}_v G_v^{13} \equiv \left[\frac{\partial h_s}{\partial x^1}\right]_{(z)}\left(\frac{\zeta}{z_{top}} - 1\right), \; \sqrt{G}_v G_v^{23} \equiv \left[\frac{\partial h_s}{\partial x^2}\right]_{(z)}\left(\frac{\zeta}{z_{top}} - 1\right). \tag{20}$$

C. Nodal DG discretization

The computational domain corresponding to $\mathcal{S}$ is the surface of a logical cube, which consists of $N_e \times N_e \times 6$ non-overlapping elements (Ω_e), where N_e is the number of elements in the x^1 or x^2 directions, such that $\mathcal{S} = \cup_e \Omega_e$. Figure 1 shows a cubed-sphere (left panel) tiled with elements; the right panel shows vertical layers in the z direction. Without loss of generality, we may describe the DG discretization on a horizontal layer (i.e., cubed-sphere surface), defined by $\zeta = \zeta_k$ of the 3D domain. Let $\mathcal{V}_h$ be a vector space of polynomials of degree up to N such that the approximate solution $\mathbf{U}_h \approx \mathbf{U}$ belongs to $\mathcal{V}_h$. Let Ω_e be a generic element on $\mathcal{S}$ with the boundary Γ_e. The weak Galerkin formulation of the problem can be obtained by multiplying Eq. 11 by the test function $\varphi_h \in \mathcal{V}_h$, and integrating by parts over Ω_e:[20]

$$\frac{d}{dt}\int_{\Omega_e}\mathbf{U}_h\,\varphi_h\,d\Omega - \int_{\Omega_e}\mathbf{F}(\mathbf{U}_h)\cdot\nabla\varphi_h\,d\Omega + \int_{\Gamma_e}\widehat{\mathbf{F}}\cdot\mathbf{n}\,\varphi_h\,d\Gamma = \int_{\Omega_e}\mathbf{S}(\mathbf{U}_h)\,\varphi_h\,d\Omega, \quad \forall\,\Omega_e \in \mathcal{S}, \tag{21}$$

where $\mathbf{n}$ is the outward-drawn unit normal vector on Γ_e, and $\widehat{\mathbf{F}}$ is the numerical flux. We use the local Lax-Friedrichs (Rusanov) numerical flux,

$$\widehat{\mathbf{F}}(\mathbf{U}_h) = \frac{1}{2}\left[(\mathbf{F}(\mathbf{U}_h^-) + \mathbf{F}(\mathbf{U}_h^+)) - \alpha_{\max}(\mathbf{U}_h^+ - \mathbf{U}_h^-)\mathbf{n}\right], \tag{22}$$

where $\alpha_{\max}$ is the maximum of the absolute value of the flux Jacobian associated with Eq. 11; $\mathbf{U}_h^-$ and $\mathbf{U}_h^+$ are the left and right state of the solution at an element edge, respectively. In order to evaluate the integrals in (21), the element Ω_e is first mapped onto the standard element $[-1,1]^2$. Usually the Gauss-Lobatto-Legendre (GLL) or Gauss-Legendre (GL) quadrature rules are employed for accurate evaluation. Here we adopt the nodal DG discretization which employs the Lagrange polynomials $h_l(\xi)$, $\xi \in [-1,1]$, $0 \le l \le N$ (with $N+1 = N_p$ solution points), as the basis functions with roots at the GLL quadrature points.[2] The horizontal grid structure is illustrated in the left panel of Fig. 1. This is a standard setup in the HOMME framework, which we adopt for HOMAM.

In a dimension-split case, the source term $\mathbf{S}$ appearing in (21) includes the vertical derivative of the flux terms. These vertical 1D flux derivatives can be approximated with a variety of high-order numerical methods; for the current work we consider 1D DG spatial discretization in the vertical z direction. The vertical DG discretization procedure is analogous to the horizontal case (21), but for K vertical 1D elements in $[h_s, z_{top}]$. We employ the GL quadrature grid for the vertical DG discretization. In Fig. 1 (right panel), the vertical GL grid structure for the HOMAM is illustrated, for which there are $K \times N_g$ independent vertical levels and each element has N_g number of GL points. The vertical DG discretization requires 1D Riemann solvers (numerical flux) and we employ the local Lax-Friedrichs numerical flux (22). Details of vertical GL grid can be found in Bao et al.[8] Thus, the total *degrees-of-freedom* for an evolving scalar field U is $6\,N_e^2 N_p^2 \times K N_g$.

Simplification of the weak form (21) leads to a system of ODEs, which can generally be written in the following form:

$$\frac{d}{dt}\,\mathbf{U}_h = L(\mathbf{U}_h) \quad \text{in} \quad (0,T), \tag{23}$$

where L indicates the DG spatial discretization.

III. Time discretization

A. Explicit method

For global NH models, the fast-moving acoustic waves together with a high aspect ratio between the horizontal and vertical spacial discretization (typically this ratio ranges between 1:100 and 1:1000, depending on the grid resolutions), impose a stringent restriction on the explicit time-step size for the resulting ODE system. Although an implicit or semi-implicit time integrator can address this issue at the cost of an expensive elliptic solver, its true cost-effectiveness is not clear at a global scale.

We consider two time integrators for solving (23), which are an explicit Runge-Kutta (RK) method and the time-split HEVI schemes. The RK method we consider is the third-order, strong stability-preserving (SSP) RK[21] scheme, hereafter referred to as the un-split RK3 scheme.

Letting $\mathbf{U}^n = \mathbf{U}_h(t)$ and $\mathbf{U}^{n+1} = \mathbf{U}(t+\Delta t)$, the three-stage explicit SSP RK3 time integration scheme can be written in the following manner:

$$\begin{aligned}
\mathbf{U}^{(1)} &= \mathbf{U}^n + \Delta t\, L(\mathbf{U}^n) \\
\mathbf{U}^{(2)} &= \frac{3}{4}\mathbf{U}^n + \frac{1}{4}\mathbf{U}^{(1)} + \frac{1}{4}\Delta t\, L(\mathbf{U}^{(1)}) \\
\mathbf{U}^{n+1} &= \frac{1}{3}\mathbf{U}^n + \frac{2}{3}\mathbf{U}^{(2)} + \frac{2}{3}\Delta t\, L(\mathbf{U}^{(2)}).
\end{aligned} \tag{24}$$

The SSP RK3 is very popular with DG discretization, however, it has a major limitation due to a severe CFL restriction. For a P^k DG method, an estimate for the CFL stability limit is given by the ratio $1/(2k+1)$, where k is the degree of the polynomial.[20] Although the horizontal CFL limit is not too restrictive with moderate order DG schemes, the tiny vertical grid spacing (Δz) can still cause severe limitations on the overall explicit time step. In order to avoid this issue, we consider a simple time-split method which employs the so-called *horizontally explicit and vertically implicit* (HEVI) approach through an operator-split procedure for the DG discretization.

B. HEVI Scheme

The spatial DG discretization $L(\mathbf{U})$ corresponding to (23) is decomposed into the horizontal L^H and vertical L^V parts such that $L(U) = L^H(\mathbf{U}) + L^V(\mathbf{U})$. For the given time interval $[t, t+\Delta t]$. The Strang-splitting

scheme has the following 3 steps:

$$\mathbf{U}_1 := \mathbf{U}_h(t), \qquad \frac{d}{dt}\mathbf{U}_1 = L^H(\mathbf{U}_1) \quad \text{in } (t, t+\Delta t/2] \tag{25}$$

$$\mathbf{U}_2 := \mathbf{U}_1(t+\Delta t/2), \qquad \frac{d}{dt}\mathbf{U}_2 = L^V(\mathbf{U}_2) \quad \text{in } (t, t+\Delta t], \tag{26}$$

$$\mathbf{U}_3 := \mathbf{U}_2(t+\Delta t), \qquad \frac{d}{dt}\mathbf{U}_3 = L^H(\mathbf{U}_3) \quad \text{in } (t+\Delta t/2, t+\Delta t], \tag{27}$$

and $\mathbf{U}_h(t+\Delta t) = \mathbf{U}_3(t+\Delta t)$.

The above HEVI algorithm follows the H-V-H cycle (another possibility is the V-H-V cycle) and each stage requires an ODE solve. The L^H component is solved explicitly using the third-order strong stability-preserving Runge-Kutta (RK) method ,[21] while the L^V component is solved implicitly using the trapezoidal rule, which is a second-order DIRK (diagonally implicit RK) method. The details of the DIRK solver can be found in Bao et al.[8] As the ODE solvers for the L^H and L^V components are at least second-order, the overall temporal accuracy of the HEVI algorithm is second-order. For atmospheric models, the computational domain is usually much wider in the horizontal direction than it is tall in the vertical, and the aspect ratio between the horizontal and the vertical grid spacing ranges from $\mathcal{O}(10^2)$ to $\mathcal{O}(10^4)$.[22] The small vertical grid spacing imposes a stringent CFL constraint on the maximum stable explicit time-step size, which makes long-term simulations computationally impractical.

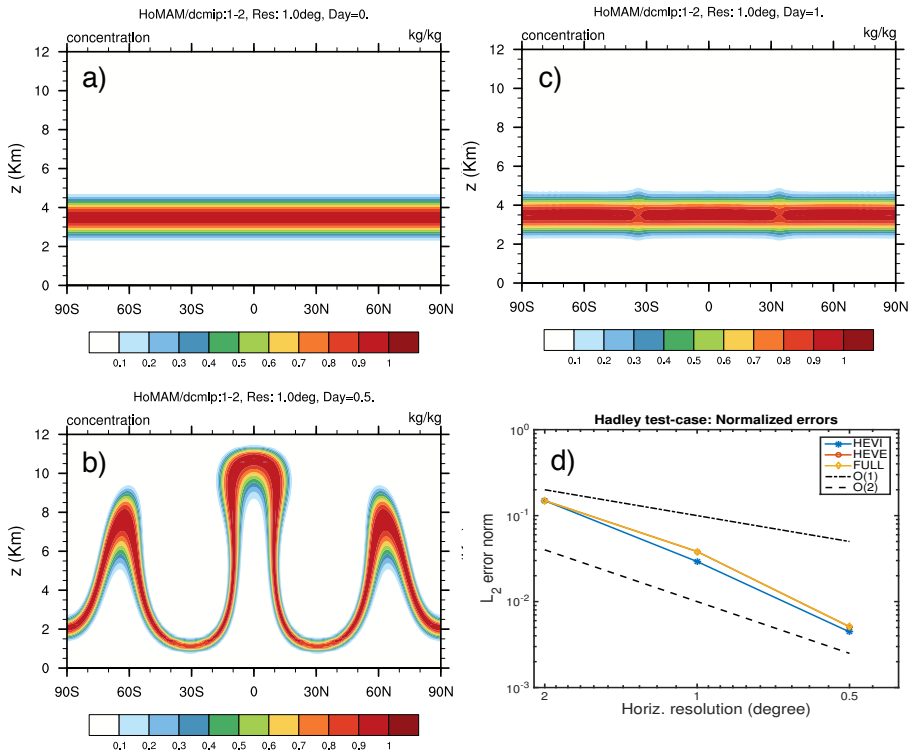

Figure 2. Vertical-meridional cross-section of the 3D tracer field q: (a) Initial value in the range $[0, 1]$, (b) at 12 hours, and (c) at 24 hours from the HOMAM simulation with a time step $\Delta t = 60$s. The horizontal resolution is $1^\circ \times 1^\circ$ ($N_e = 30, N_p = 4$) with 60 vertical levels ($K = 15, N_g = 4$). The panel (d) shows the convergence of the ℓ_2 error norm after 1 day of simulation with explicit and HEVI time stepping methods.

For the HEVI algorithm, since the vertical component is treated implicitly, the CFL constraint is relaxed and only limited by the much larger horizontal grid spacing. Therefore, the maximum allowed time-step size of the HEVI algorithm is greatly increased from the explicit time-step size, depending on the horizontal-vertical aspect ratio. Moreover, the widely used horizontal domain decomposition maintains columns on a single processor so that the data of the vertical component L^V is locally accessible. In this way, the implicit component can be solved efficiently without introducing additional inter-processor communication overhead. The HEVI algorithm permits much larger time-step size and does not impede the near optimal scalability of

the HOMME environment. The vertical implicit solve is the dominating factor of the overall computational cost of the HEVI algorithm. The Newton-Krylov method is adopted to solve the nonlinear system resulting from the 1D vertical implicit solve. If the nonlinear function is simple enough, the Jacobian matrix of the nonlinear system can be computed and the resulting block tridiagonal system can be solved cheaply. Otherwise, the Jacobian-free Newton-Krylov (JFNK) method can be used as an alternative.[8] The HEVI algorithm is an efficient and practical choice for the time integration schemes for global non-hydrostatic atmospheric modeling. This will be demonstrated with the following benchmark test cases.

IV. Numerical Results

The Dynamical Core Model Intercomparison Project (DCMIP),[10] provides a set of benchmark test cases for validating global NH atmospheric models. These tests include 3D advection tests with known analytic solutions, "small planet" simulations (with the Earth's radius reduced), and various gravity wave and baroclinic instability tests. For the numerical tests considered herein, we have used the following grid configuration for HOMAM, as illustrated in Fig.1. The 2D horizontal spherical elements employs $(N_p \times N_p)$ GLL quadrature points with $N_p = 4$, and the vertical 1D elements use $N_g = 4$, GL quadrature points on each element.

A. 3D Advection

We first consider a 3D advection test with non-divergent deformational flow for which the final solution is known, as it is designed to be the initial condition, for facilitating convergence studies. This test is also referred to as the "Hadley" test in the DCMIP test suite.[10] The wind fields are designed so that the flow reverses itself halfway (at 12 hours) through the simulation and returns the tracers to their initial position, therefore, the exact solution is known at the end of the 24-hour run. Note that for this test we solve only the transport Eq. (10), where q is initially prescribed as a quasi-smooth cosine profile.[11,9]

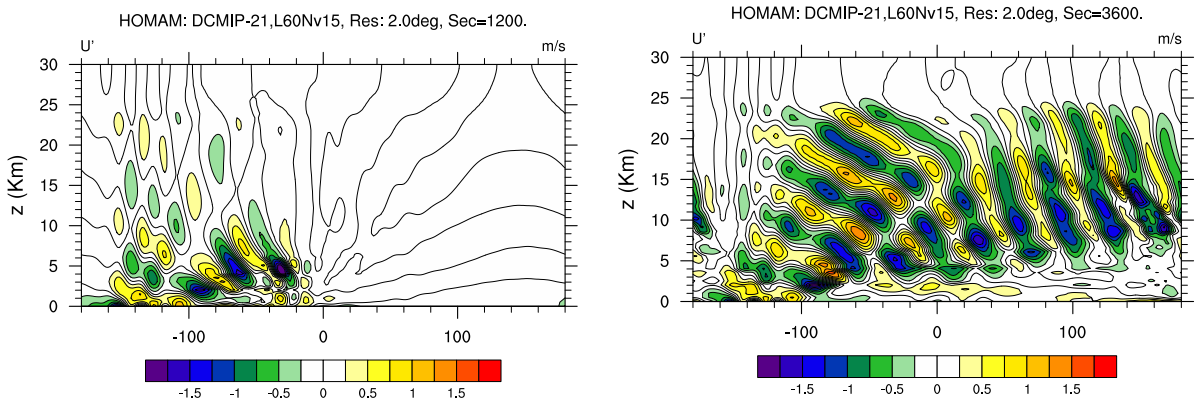

Figure 3. Simulated results for non-hydrostatic mountain waves over a 3D Schär-type mountain. The left and right panels show vertical slices of horizontal wind perturbation (u') along the equator after 1200 **and** 3600 **seconds, respectively. The simulation was performed with a horizontal resolution of** 2°**, with 60 vertical levels and** $\Delta t = 0.20$s

The simulated result with HOMAM is shown in Fig. 2, where panels (a) and (c) show the meridional cross-section of initial and final solutions, respectively, at a horizontal resolution $1^\circ \times 1^\circ$. The maximum deformation of the field occurs at 12 hours, as shown in Fig. 2(b). After 24 hours into the simulation, the tracer field closely resembles its initial value, however, some deviations are noticeable where the deformation (stretching) is maximum. The normalized standard $\ell_1, \ell_2, \ell_\infty$ errors were computed and compared with other establish models.[9] A combined horizontal-vertical convergence rate with HOMAM was found to be greater than 2nd-order, which is comparable or better than those reported by other modeling groups.[11,9]

Our particular interest for this test is to investigate the impact of horizontal-vertical spatial splitting on the accuracy of the scheme. Figure 2 panel (d) shows the l_2 error convergence for the Hadley test with explicit (full) and HEVI time integrators, with a fixed small time step of $\Delta t = 6$ s and doubling the 3D spatial resolution. Figure 2(d) indicates that the convergence rate is approximately 2nd-order, which is also

consistent with the Strang-type time-splitting.[9] Figure 2(d) also shows that the split time stepping with various options (H-V-H or V-H-V cycles) has a minimal effect on the error norms when compared with the explicit RK scheme.

B. Flow over a 3D Mountain

In order to examine the ability of the solver to represent non-hydrostatic effects, a mountain-wave test over a non-smooth mountain is conducted. The main purpose of this test is to study the impact of orography on an atmosphere at rest. This is particularly interesting for models with terrain-following, height-based vertical coordinates, which invariably introduces numerous metric terms. The mountain profile consists of concentric 3D circular (Schär-type[23]) mountains with a maximum height of 2 km. In order to ensure that the simulated response displays non-hydrostatic features, the radius of the Earth is scaled for this test so that the simulation is in the non-hydrostatic domain. The radius of the Earth is reduced by a factor of 500 and Coriolis effects are neglected. In addition, the test requires the specification of Rayleigh friction in a rather thick sponge layer that occupies one third of the domain near the model top. It is needed to absorb upward propagating gravity waves and prevent their reflection at the model top. We have adopted the parameters recommended in the DCMIP test suite.[10] The 'no-flux' bottom boundary condition is imposed such that the normal component of velocity vanishes at the boundary. In the ζ-coordinates this implies $\tilde{w} = 0$ along the bottom boundary.[8] The model captures the mountain-induced gravity wave propagation as shown in Fig. 3, and the results are comparable to those of the reference results presented in DCMIP with several models.[10]

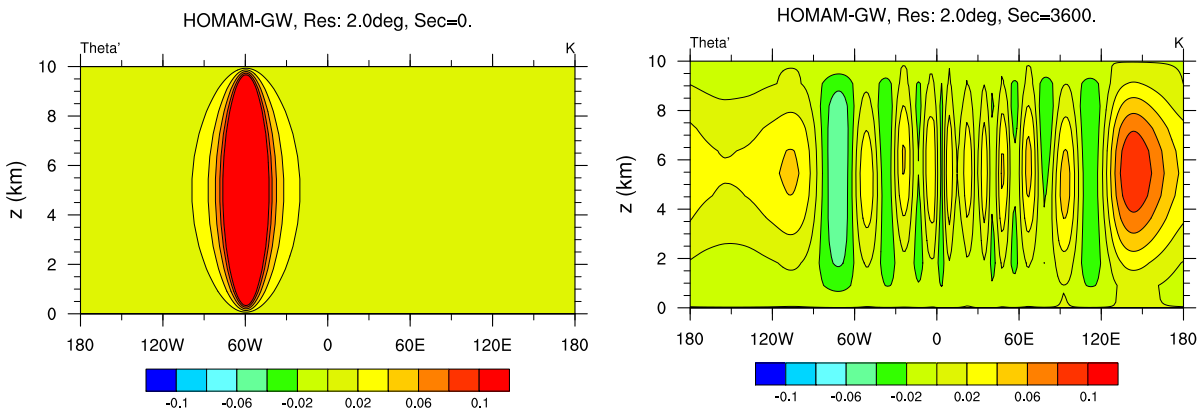

Figure 4. Simulation of the 3D non-hydrostatic gravity wave propagation on a reduced planet using the HOMAM dynamical core. The left panel shows the initial potential temperature perturbation (2D vertical slice along the equator), which triggers the evolution of gravity waves as shown in the right panel after 3600 s. The horizontal resolution is 2° with 12 vertical levels and $\Delta t = 0.25$ s with the SSP RK3 method.

C. Inertia-Gravity Wave test

This is an idealized test involving full 3D nonlinear dynamics, where the initial state is hydrostatically balanced. This test examines the response of the model to short time-scale wave motion triggered by a local perturbation, which provides an excellent tool for testing the model dynamics. For this test an overlaid potential temperature perturbation triggers evolution of gravity waves over a 1-hour period on a reduced (shrunken) planet. The gravity wave test on a reduced-size Earth discriminates between hydrostatic and non-hydrostatic responses, therefore, the radius of the Earth is reduced by a factor of 125, and the angular velocity is kept at zero. Figure 4 shows the initial and final simulated results of the 3D NH inertia-gravity wave test.

The preliminary results with the HOMAM are encouraging, and are comparable to those of the DCMIP benchmark results produced with established models. Figure 5 (right panel) shows the HOMAM simulation results with the NH gravity wave test as recommended in the DCMIP test suite. Since the time-step size of the HEVI algorithm is constrained by the horizontal motion, we choose Δt=0.25 s for the numerical experiments. The contour plots of the fields of the potential temperature perturbation at $t_T = 3600$ s are shown for different vertical levels in Fig. 5. For the HEVI algorithm, we see that the potential temperature

perturbation fields at $t = 3600$ s are virtually identical when using 12, 24 and 60 vertical levels. Minor differences are observed between the results of the SSP-RK3 scheme and the HEVI algorithm. However, the quality of all contour plots is very close to other NH models in the literature, such as ICON-IAP and ENDGame.[10]

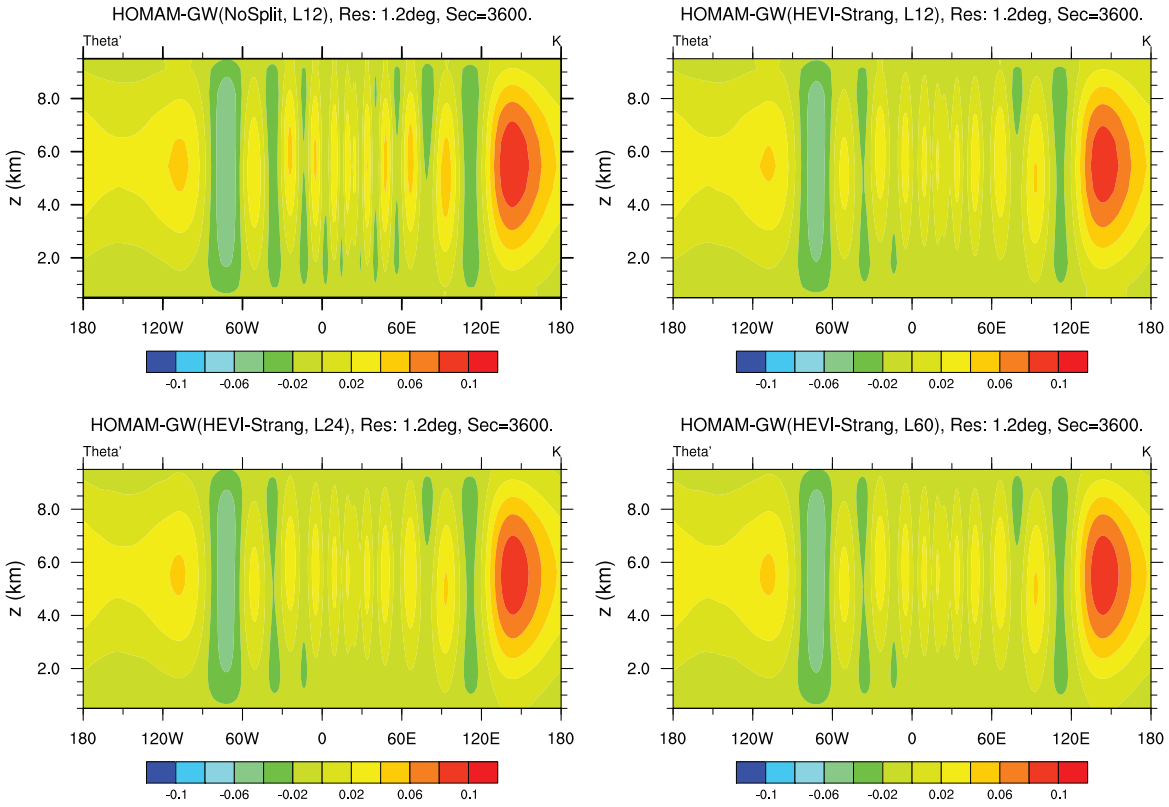

Figure 5. 3D non-hydrostatic gravity wave simulation with HOMAM with varying vertical levels. Contour plot of the potential temperature perturbation field on a grid with $1.2^\circ \times 1.2^\circ$ resolution in the horizontal. 12, 24 and 60 vertical levels are tested for the HEVI algorithm. $\Delta t = 0.25$ s for all the experiments. The result using 12 vertical levels and SSP-RK3 scheme is used as a reference solution.

To test the strong scalability performance of the HEVI algorithm, a numerical experiment is run on a grid with $0.23^\circ \times 0.23^\circ$ in the horizontal and $\Delta z \simeq 166.7$ m ($N_e = 128, N_p = 4, N_v = 15, N_v = 4$). The strong scaling results of the HEVI algorithm are shown in Fig. 6. This experiment is only simulated for $t_T = 1000$ s due to the excessive computational cost. Since $\Delta t_{HEVI} = \Delta t_{explicit}$, there is no benefit by using the HEVI algorithm, but the overall scalability performance of the scheme can still be evaluated. We can see that both the HEVI algorithm and SSP-RK3 scheme show nearly linear speedup. This demonstrates that the HEVI algorithm does not impede the nearly optimal scalability of the HOMME framework.

V. Conclusion

A 3D non-hydrostatic (NH) model (HOMAM) has been developed by extending the hydrostatic dynamical core HOMME. The model uses a discontinuous Galerkin (DG) spatial discretization on the cubed sphere. The vertical grid system follows a terrain-following vertical coordinate. A dimension split strategy (2D + 1D) is used for the spatial discretization, combining the 2D horizontal elements on the cubed-sphere surface and 1D vertical elements in the terrain-following height-based coordinate. Various time-stepping schemes have been tested for 3D advection in the global atmospheric dynamical core HOMAM. The time integrators are the horizontally explicit and vertically implicit (HEVI) algorithm and an un-split third-order Runge-Kutta scheme. One challenging advection test and two 3D NH tests from the DCMIP test suite are used for validating the schemes. The convergence shows a second-order accuracy with a smooth scalar field,

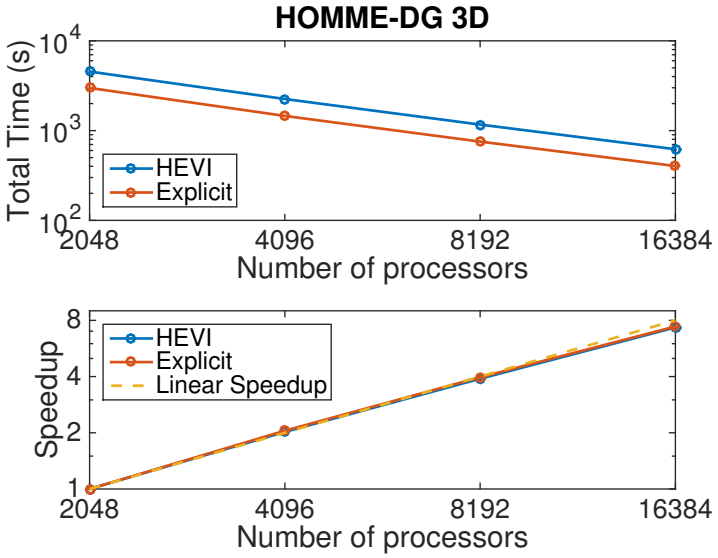

Figure 6. Strong scaling results of the HEVI algorithm and SSP-RK3 scheme

irrespective of a particular time integrator. The model successfully simulates mountain-induced gravity waves and horizontally propagating NH gravity waves. The split schemes work well and results are comparable with other published results. The scaling results show that HEVI implementation does not impede the scalability of the HOMME framework.

Appendix

The metric tensor for the (x^1, x^2, z) curvilinear system based on the gnomonic transformation and the shallow-atmosphere approximation is defined as,

$$G_{ij} = \begin{bmatrix} G_{11} & G_{12} & 0 \\ G_{21} & G_{22} & 0 \\ 0 & 0 & 1 \end{bmatrix},$$

such that the Jacobian of the transformation $\sqrt{G} = |G_{ij}|^{1/2} = \sqrt{G_h}$.

The Christoffel symbols associated with the transformation appearing in Eq. (8) are formally defined as follows:

$$\Gamma^i_{jk} = \frac{1}{2} G^{il} \left[\frac{\partial G_{kl}}{\partial x^j} + \frac{\partial G_{jl}}{\partial x^k} - \frac{\partial G_{kj}}{\partial x^l} \right], \tag{28}$$

and for the current application they have the following explicit form:

$$\Gamma^1_{11} = \frac{2\tan(x^1)\tan^2(x^2)}{\mu^2}, \quad \Gamma^1_{12} = -\frac{\tan(x^2)\sec^2(x^2)}{\mu^2}, \quad \Gamma^1_{22} = 0$$

$$\Gamma^2_{11} = 0, \quad \Gamma^2_{12} = -\frac{\tan(x^1)\sec^2(x^1)}{\mu^2}, \quad \Gamma^2_{22} = \frac{2\tan^2(x^1)\tan(x^2)}{\mu^2}.$$

The explicit forms of the source terms M^1_Γ, M^2_Γ are defined as

$$M^1_\Gamma = \Gamma^1_{11}(\rho u^1 u^1 + p' G^{11}_h) + 2\Gamma^1_{12}(\rho u^1 u^2 + p' G^{12}_h) + \Gamma^1_{22}(\rho u^2 u^2 + p' G^{22}_h)$$
$$M^2_\Gamma = \Gamma^2_{11}(\rho u^1 u^1 + p' G^{11}_h) + 2\Gamma^2_{12}(\rho u^1 u^2 + p' G^{12}_h) + \Gamma^2_{22}(\rho u^2 u^2 + p' G^{22}_h).$$

Notes on the $(x^1, x^2, z) \rightarrow (x^1, x^2, \zeta)$ transform

Let us consider the u^1-equation first. The u^1-momentum equation for the perturbed Euler system can be written in terms of the horizontal metric terms $\sqrt{G}_h$ and G_h^{ij} associated with the cubed-sphere mapping shown below:

$$\frac{\partial \rho u^1}{\partial t} + \frac{1}{\sqrt{G}}\left\{\frac{\partial}{\partial x^1}[\sqrt{G}(\rho u^1 u^1 + G^{11}p')] + \frac{\partial}{\partial x^2}[\sqrt{G}(\rho u^1 u^2 + G^{12}p')] + \frac{\partial}{\partial x^3}[\sqrt{G}(\rho u^1 u^3)]\right\}$$
$$+\Gamma^1_{11}(\rho u^1 u^1 + p'G^{11}) + 2\Gamma^1_{12}(\rho u^1 u^2 + p'G^{12}) + \Gamma^1_{22}(\rho u^2 u^2 + p'G^{22})$$
$$= f\sqrt{G}(G^{12}u^1 - G^{11}u^2). \tag{29}$$

This can be simplified as follows in the (x^1, x^2, z) cubed-sphere shallow-atmosphere formulation:

$$\frac{\partial \sqrt{G}_h \rho u^1}{\partial t} + \frac{\partial}{\partial x^1}[\sqrt{G}_h(\rho u^1 u^1 + G_h^{11}p')] + \frac{\partial}{\partial x^2}[\sqrt{G}_h(\rho u^1 u^2 + G_h^{12}p')] + \frac{\partial}{\partial z}[\sqrt{G}_h(\rho u^1 w)]$$
$$= f^1 - \Gamma^1_M \equiv S^1_u, \tag{30}$$

where the suffix h indicates horizontal metric terms resulting from the cubed-sphere mapping. f^1 and Γ^1_M are the Coriolis term and geometric term (or cubed-sphere curvature term) which constitute the source S^1_u for the u^1-momentum equation.

Our goal is to further transform Eq. (30) into the (x^1, x^2, ζ) system by utilizing the following differential transforms.[19] For an arbitrary scalar $\psi = \psi(x^1, x^2, z)$, we can write

$$\begin{aligned}
\sqrt{G}_v \frac{\partial \psi}{\partial x^1} &= \frac{\partial(\sqrt{G}_v \psi)}{\partial x^1} + \frac{\partial(\sqrt{G}_v G_v^{13}\psi)}{\partial \zeta} \\
\sqrt{G}_v \frac{\partial \psi}{\partial x^2} &= \frac{\partial(\sqrt{G}_v \psi)}{\partial x^2} + \frac{\partial(\sqrt{G}_v G_v^{23}\psi)}{\partial \zeta} \\
\sqrt{G}_v \frac{\partial \psi}{\partial z} &= \frac{\partial \psi}{\partial \zeta}.
\end{aligned}$$

Now multiplying (30) by $\sqrt{G}_v$ and using the definition $\sqrt{G} = \sqrt{G}_h\sqrt{G}_v$, we have:

$$\frac{\partial \sqrt{G} \rho u^1}{\partial t} + \sqrt{G}_v \frac{\partial}{\partial x^1}[\sqrt{G}_h(\rho u^1 u^1 + G_h^{11}p')] + i\frac{\partial}{\partial x^2}[\sqrt{G}_h(\rho u^1 u^2 + G_h^{12}p')] + \sqrt{G}_v \frac{\partial}{\partial z}[\sqrt{G}_h(\rho u^1 w)]$$
$$= \sqrt{G}_v S^1_u. \tag{31}$$

Using the above differential transform for ψ we get

$$\frac{\partial \sqrt{G} \rho u^1}{\partial t} + \frac{\partial}{\partial x^1}[\sqrt{G}(\rho u^1 u^1 + G_h^{11}p')] + \frac{\partial}{\partial x^2}[\sqrt{G}(\rho u^1 u^2 + G_h^{12}p')] +$$
$$\frac{\partial}{\partial \zeta}[\sqrt{G}_h(\rho u^1 w)] + \frac{\partial}{\partial \zeta}[\sqrt{G}_h\sqrt{G}_v G_v^{13}(\rho u^1 u^1 + G_h^{11}p')] + \frac{\partial}{\partial \zeta}[\sqrt{G}_h\sqrt{G}_v G_v^{23}(\rho u^1 u^2 + G_h^{12}p')]$$
$$= \sqrt{G}_v S^1_u, \tag{32}$$

$$\frac{\partial \sqrt{G} \rho u^1}{\partial t} + \frac{\partial}{\partial x^1}[\sqrt{G}(\rho u^1 u^1 + G_h^{11}p')] + \frac{\partial}{\partial x^2}[\sqrt{G}(\rho u^1 u^2 + G_h^{12}p')] +$$
$$\frac{\partial}{\partial \zeta}[\sqrt{G}_h \rho u^1(w + \sqrt{G}_v G_v^{13}u^1 + \sqrt{G}_v G_v^{23}u^2) + \sqrt{G}_h(\sqrt{G}_v G_v^{13} G_h^{11}p' + \sqrt{G}_v G_v^{23} G_h^{12}p')$$
$$= \sqrt{G}_v S^1_u. \tag{33}$$

By using the relation $\sqrt{G}_v\tilde{w} = w + \sqrt{G}_v G_v^{13}\,u^1 + \sqrt{G}_v G_v^{23}\,u^2$, we get the following simplification:

$$\frac{\partial \sqrt{G} \rho u^1}{\partial t} + \frac{\partial}{\partial x^1}\left[\sqrt{G}(\rho u^1 u^1 + G_h^{11}p')\right] + i\frac{\partial}{\partial x^2}\left[\sqrt{G}(\rho u^1 u^2 + G_h^{12}p')\right] +$$
$$\frac{\partial}{\partial \zeta}\left[\sqrt{G}\rho u^1\tilde{w} + \sqrt{G}(G_v^{13}G_h^{11}\,p' + G_v^{23}G_h^{12}\,p')\right] = \sqrt{G}_v S^1_u. \tag{34}$$

By symmetry, we can write the u^2-equation as

$$\frac{\partial\sqrt{G}\rho u^2}{\partial t} + \frac{\partial}{\partial x^1}\left[\sqrt{G}(\rho u^2 u^1 + G_h^{21}p')\right] + \frac{\partial}{\partial x^2}\left[\sqrt{G}(\rho u^2 u^2 + G_h^{22}p')\right] + \frac{\partial}{\partial \zeta}\left[\sqrt{G}\rho u^2\tilde{w} + \sqrt{G}(G_v^{13}G_h^{21}\,p' + G_v^{23}G_h^{22}\,p')\right] = \sqrt{G}_v S_u^2. \tag{35}$$

References

[1]Dennis, J. M., Edwards, J., Evans, K. J., Guba, O., Lauritzen, P. H., Martin, A. A., St-Cyr, A., Taylor, M. A., and Worely, P. H., "CAM-SE: A scalable spectral element dynamical core for the Community Atmosphere Model," *International Journal of High Performance Computing Applications*, Vol. 26, 2012, pp. 74–89.

[2]Nair, R. D., Choi, H.-W., and Tufo, H. M., "Computational aspects of a scalable high-order Discontinuous Galerkin atmospheric dynamical core," *Computers and Fluids*, Vol. 38, 2009, pp. 309–319.

[3]Skamarock, W. C., Klemp, J. B., Duda, M. G., Flower, L. D., Park, S.-H., and Ringler, T. D., "A Multiscale Nonhydrostatic Atmospheric Model Using Centroidal Voronoi Tesselations and C-Grid Staggering," *Mon. Wea. Rev.*, Vol. 140, 2012, pp. 3090–3105.

[4]Simmaro, J. and Hortal, M., "A semi-implicit non-hydrostatic dynamical kernel using finite elements in the vertical discretization," *Q. J. R. Meteorol. Soc.*, Vol. 138, 2012, pp. 826–839.

[5]Zagal, G., Ripodas, D. R. P., and Baldauf, M., "The ICON (ICOsahedral Non-hydrostatic) modelling framework of DWD and MPI-M: Description of the non-hydrostatic dynamical core," *Q. J. R. Meteorol. Soc*, 2014, pp. 1–17, DOI: 10.1002/qj.2378.

[6]Brdar, S., Baldauf, M., Dedner, A., and Klöfkorn, R., "Comparison of dynamical cores for NWP models: comparison of COSMO and Dune," *Theor. Comput. Fluid Dyn.*, Vol. 27, 2013, pp. 453–472.

[7]Kelley, J. F. and Giraldo, F. X., "A Continuous and discontinuous Galerkin methods for a scalable three-dimensional nonhydrostatic atmospheric model: Limited-area mode," *J. of Comput. Phys.*, Vol. 231, 2012, pp. 7988–8008.

[8]Bao, L., Klöfkorn, R., and Nair, R. D., "Horizontally Explicit and Vertically Implicit (HEVI) Time Discretization Scheme for a Discontinuous Galerkin Nonhydrostatic Model," *Mon. Wea. Rev.*, Vol. 143, 2015, pp. 972–990, doi:10.1016/j.procs.2015.05.471.

[9]Nair, R. D., Bao, L., and Toy, M. D., "A Time-Split Discontinuous Galerkin Transport Scheme for Global Atmospheric Model," *Procedia Computer Science*, Vol. 51, 2015, pp. 2056–2065, doi:10.1016/j.procs.2015.05.471.

[10]Ullrich, P. A., Jablonowski, C., Kent, J., Reed, K. A., Lauritzen, P. H., Nair, R. D., and Taylor, M. A., "https://www.earthsystemcog.org/projects/dcmip-2012/," *The 2012 Dynamical Core Model Intercomparison Project*, 2012.

[11]Kent, J., Ullrich, P. A., and Jablonowski, C., "Dynamical core model intercomparison project: Tracer transport test cases," *Q. J. Roy. Meteol. Soc.*, Vol. 140, 2014, pp. 1279–1293.

[12]Bacon, D., Ahmad, N., Boybeyi, Z., Dunn, T., Hall, H., Lee, P., Sarma, R., Turner, M., Waight, K., Young, S., and Zack, J., "A dynamically adapting weather and dispersion model: the operational multiscale environment model with grid adaptivity (OMEGA)," *Mon. Wea. Rev.*, Vol. 128, 2000, pp. 2044–1144.

[13]Skamarock, W. C. and Klemp, J. B., "A time-split nonhydrostatic atmospheric model for weather research and forecasting applications," *J. Comput. Phys.*, Vol. 227, 2008, pp. 3465–3485.

[14]Sadourny, R., "Conservative finite-difference approximations of the primitive equations on quasi-uniform spherical grids," *Mon. Wea. Rev.*, Vol. 100, 1972, pp. 136–144.

[15]Nair, R. D., Thomas, S. J., and Loft, R. D., "A Discontinuous Galerkin global shallow water model," *Mon. Wea. Rev.*, Vol. 133, 2005, pp. 876–888.

[16]Warsi, Z. U. A., *Fluid Dynamics: Theoretical and Computational Approaches, Third Edition*, CRC Press, 1992.

[17]Bao, L., Nair, R. D., and Tufo, H. M., "A mass and momentum flux-form high-order Discontinuous Galerkin shallow water model on the cubed-sphere," *J. Comput. Phys.*, Vol. 271, 2014, pp. 224–243.

[18]Gal-Chen, T. and Sommerville, R. C., "On the use of a coordinate transformation for the solution of Navier-Stokes," *J. Comput. Phys.*, Vol. 17, 1975, pp. 209–228.

[19]Clark, T. L., "A small-scale dynamics model using a terrain-following coordinate transformation," *J. Comput. Phys.*, Vol. 24, 1977, pp. 186–215.

[20]Cockburn, B., "An introduction to the Discontinuous-Galerkin method for convection-dominated problems," *Lecture Notes in Mathematics: Advanced Numerical Approximation of Nonlinear Hyperbolic Equations*, edited by A. Quarteroni, Vol. 1697, Springer, 1997, pp. 151–268.

[21]Gottlieb, S., Shu, C.-W., and Tadmor, E., "Strong Stability-Preserving high-order time discretization methods," *SIAM Review*, Vol. 43, No. 1, 2001, pp. 89–112.

[22]Lock, S. J., Wood, N., and Weller, H., "Numerical analyses of Runge-Kutta implicit-explicit schemes for horizontally explicit, vertically implicit solutions of atmospheric models," *Quarterly Journal of the Royal Meteorological Society*, Feb. 2014, pp. n/a–n/a.

[23]Schar, C., Leuenberger, D., Fuhrer, O., Luthic, D., and Girard, C., "A new terrain-following vertical coordinate formulation for atmospheric prediction models," *Mon. Wea. Rev.*, Vol. 130, 2002, pp. 2459–2480.